

Chapter 2

The Technique: Resonant X-ray Scattering

2.1 Introduction

The experimental technique used throughout this thesis to investigate the ordered states of the TMO heterostructures is resonant soft X-ray scattering (RSXS). In general, wave scattering techniques provide a non-destructive way to obtain correlation function information involving a large number of scattering entities. Non-resonant X-ray scattering served the framework for crystal structure determination when the tube source was developed. Later, other methods emerged including electron and neutron scattering, which with a charge or spin attribute, can interact with solid state matter and render precise location information about nuclear, ionic and magnetic scatterers. However, these can have limitations including non-element specificity, narrow penetration depths, low fluxes available, need for bulk samples, etc. Some of these limitations are overcome by the use of X-rays.

Resonant elastic X-ray scattering (REXS) in general refers to a technique based on tuning the X-ray photon's energy to match the value required to excite an inner-shell electron into a valence state of the atom of interest. While non-resonant scattering can provide insight beyond structural origin, e.g. magnetic or orbital [1, 2], the cross sections involved are small, so detailed refinements remain a technical challenge. This is where the REXS technique is important to solid state physics. We will later show how the scattering cross section is dramatically enhanced by tuning the incoming photon energies to the absorption transitions. Thus, this class of experiments combines the X-ray absorption (XAS) with diffraction, i.e. a Fourier transform of spatial modulations sensitive to electronic details. However, tuning to any edge may not be sufficient to enhance the cross section into a detectable range. Instead, judiciously chosen dipole-allowed transitions into final states near the Fermi level can result in a larger cross section, which directly ties into the electrons responsible for the macroscopic physics of the material. For 3d-TMOs, the appropriate dipole-allowed transition is $2p \rightarrow 3d$, the $L_{2,3}$ -edges, which falls within the energy range of 200–2000 eV, the so-called soft X-rays. Although this wavelength range (~ 1 nm) drastically limits the accessible reciprocal space region, some ordered superstructures in TMOs reach the

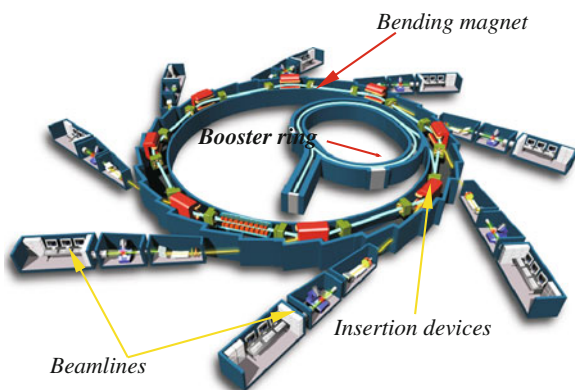


Fig. 2.1 A schematic of a synchrotron radiation source: electrons are injected through the booster ring, then accelerated along the bending magnets, and/or insertion devices. The radiation is collected for research at the beamline end-stations. Figure adapted from Wikimedia Commons

nm-scale, making RSXS the tool of choice to investigate the details of possible spin, orbital, and charge order. For a review on recent developments of the technique, see Refs. [3, 4].

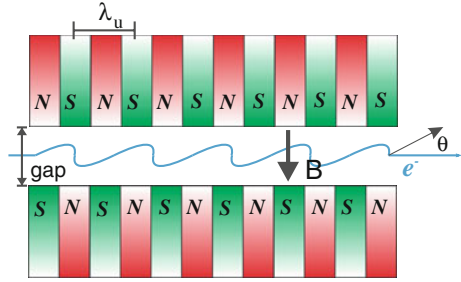
Despite its great assets, the RSXS method has its challenges and disadvantages. The wavelength scale is rather large, limiting the momentum transfer. In addition, due to the large absorption coefficient of air at these energies, sample environments must be held in vacuum. Moreover, generating the X-rays is not as simple as in non-resonant diffraction. This is where the progression of synchrotron based sources provided useful.

2.2 X-ray Sources: Synchrotron Radiation

REXS and particularly RSXS are techniques closely connected to the development of synchrotron radiation light sources. The synchrotron emerged as an accidental discovery in particle accelerator physics [5–7], but has since developed into sources for modern X-ray techniques. The last five decades have spawned 4 generations of synchrotron light sources, all of which rely on the notion of accelerating a charged electron into relativistic speeds within curved paths. In the first 3 generations, an accelerator drives electrons into closed orbits by applying magnetic fields. The 3rd generation is characterized by the inclusion of straight “insertion devices” within the ring.¹ A schematic of a typical 3rd-generation synchrotron layout is shown in Fig. 2.1, whose components will be explained in the following.

¹ The 4th generation of these light sources are linear accelerators, or “free electron lasers”, which do not force the electrons in circular orbits but in linear paths.

Fig. 2.2 The basic principle of an insertion device, where alternating magnetic dipoles accelerate the electrons in a oscillating path. These emit more intense radiation compared to the bending magnet. The oscillations occur outside the paper's plane



The electrons are first ramped into relativistic velocities in the booster ring. Then, the “storage rings” maintain the electrons in a high-energy orbit, replenishing their energy as they emit a special kind of light. This source kind is termed “bending magnet” radiation, and has several unique features like a high brilliance (a term defined to contain the degree of collimation, beam size, intensity, and spectral distribution), a broad and tunable emission energy range and a high degree of polarization of the light. These characteristics are a combined result of the relativistic movement of the electrons around a curved path and the relativistic Doppler effect. The conventional Doppler shift of an emitting electron has a spherical effect, where wavelength is increased when the moving object is going towards the viewer, and decreasing when moving away from it. The relativistic Doppler effect, on the other hand, and due to the Lorentz transformations, causes the radiation to be strongly blue-shifted and the direction of emittance is highly concentrated in the forward direction. The divergence of the beam under a relativistic Doppler blue-shift is roughly given by mc^2/E_e , where m , E_e , c are the mass and energy of the electron, and the speed of light in vacuum, respectively. A characteristic energy defined as $\hbar\omega_c$ [keV] = $0.665 E_e^2$ [GeV] B [Tesla] is given by the conditions of a bending magnet. For example, the BESSY synchrotron in Berlin, Germany operates at 1.7 GeV, optimized for the soft X-ray regimes. This quantity varies depending on the research focus of the synchrotron.

A large improvement in generating synchrotron light was achieved with the conception of insertion devices, which can offer more brilliance, sharp tunable energy spectra, partial temporal and spatial coherence, and full polarization control from the source. These are essentially arrays of alternating magnets which drive relativistic electrons into an oscillatory path. The two important parameters of an insertion device are the magnetic field B and the magnet period λ_u , as shown in Fig. 2.2.

A dimensionless parameter used to discern between insertion device types, $K = \frac{eB\lambda_u}{2\pi\beta m_e c}$, classifies the deflection path of the electron. There are two types of insertion devices: undulators ($K \lesssim 1$) and wigglers ($K \gg 1$). Wigglers operate with high magnetic fields with a large number N of period repetitions. They can be regarded as a superposition of bending magnet radiators, so the intensity becomes $I \propto N$. Undulators, on the other hand, produce a coherent superposition of the emitted light, so $I \propto N^2$ but concentrated within a narrow energy range. The energy spectral range $\Delta\omega/\omega$ of an undulator source can be several orders of magnitude reduced with respect

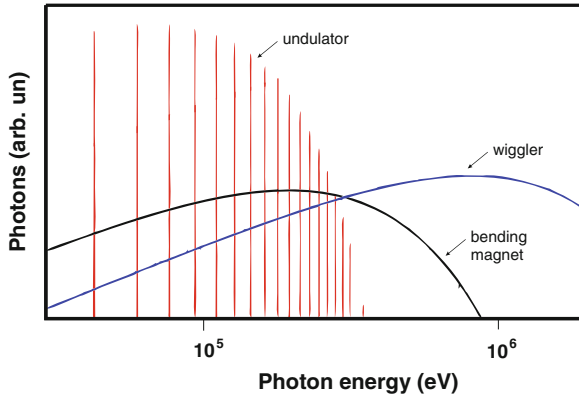


Fig. 2.3 A schematic of an undulator’s discrete spectrum compared to the continuous wiggler and bending magnet spectra. Image adapted from [8]

to the bending magnet radiation, resulting in a much higher brilliance. Because of the sinusoidal nature of the electron’s path, the energy an undulator produces from a single electron inherently comes in a discrete value, and its subsequent odd harmonics.² The expression for this energy is given by

$$E_n(\text{eV}) = n \frac{950 E_e^2(\text{GeV})}{\lambda_u(\text{cm})(1 + K_{eff}^2/2 + \gamma^2 \theta^2)}, \quad (2.1)$$

where γ is the relativistic factor of the electrons, $K_{eff} = 0.934 \lambda_u(\text{cm}) B(T)$, θ is the polar angle from the undulator axis (Fig. 2.2), and n is the odd harmonic.

Undulators can change the gap between magnetic dipoles, modifying the magnetic field strength and thus K . This shifts the peaks in the energy spectra horizontally, optimizing the brightness for a certain energy range of interest. The resulting spectral brightness of an undulator compared to bending magnets and wigglers is shown in Fig. 2.4. Furthermore, “helical undulators” allow to horizontally shift the magnetic dipoles inducing a spiral motion of the electron wave train. This can result in variable polarization of the emitted light, which can adopt linear (with any angle from vertical to horizontal) or elliptical (positive and negative) states.

2.3 Resonant Scattering

The field of REXS emerged in the mid 1970s, once the technical challenge of producing tunable, bright X-ray sources was overcome. It began with a discussion of so-called “anomalous scattering” [9], which was a term referring to finite intensities emerging around otherwise forbidden reflections when the photon energy neared an

² However, the even harmonics do also exist in the off-axis radiation, that is, the radiation emitted at a small angle with respect to the tangential forward direction of the electron.

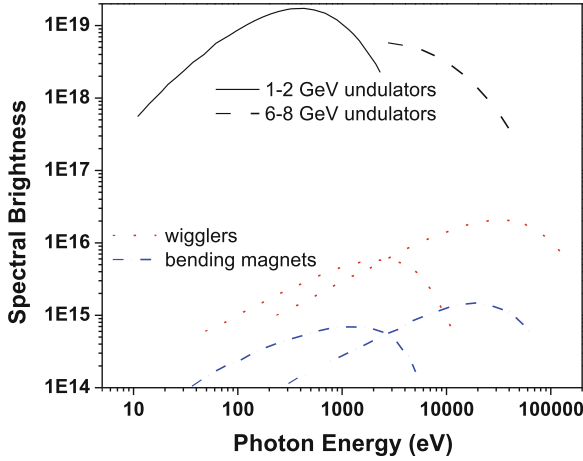


Fig. 2.4 A comparison between the spectral brightness of bending magnets, wigglers, and undulators

absorption edge. Subsequent seminal work on REXS included Hannon et al. [10], Carra and Thole [11], Hill and McMorow [12], etc., which climaxed during the International Conference on Anomalous Scattering in Malente, Germany, in 1992 [13]. During these stages, the importance of calculating resonant scattering factors was realized, so the theoretical framework to understand resonant XAS was developed alongside, which is summarized in papers like [14] and others. In this section, we will lay out the theoretical background of REXS, including a brief introduction to X-ray physics, general remarks about the interaction of light and matter, the scattering factor, its connection to XAS, charge, magnetic and orbital scattering, and finalize with a description of realistic experimental aspects. This section was written collecting Refs. [3, 4, 10, 15–18] and others therein.

2.3.1 Basic Principles of X-ray Physics

The interaction of X-rays with solid state matter is a field with an enormous utility and widespread interest. While a thorough introduction can be found in [6], we begin our discussion with few words on absorption and diffraction. For non-resonant, elastic scattering from a single atom, the classical description serves a valid framework. The atom is modeled as an electron density of spherical symmetry $\rho(\vec{r})$. The unequal optical path lengths traveled by different wavefronts, $\vec{q}_1 \cdot \vec{r}_1 \neq \vec{q}_2 \cdot \vec{r}_2$ (where the momentum transfer $\vec{q} \equiv \vec{k} - \vec{k}'$), will result in a phase shift between waves, i.e. diffraction. The diffraction event will integrate over all waves scattered from each position \vec{r}_i :

$$f(\vec{q}) = \int r_0 \rho(\vec{r}) e^{i\vec{q} \cdot \vec{r}} d\vec{r}, \quad (2.2)$$

where we have introduced the atomic form factor $f(\vec{q})$. The full atomic form factor is, in general, energy dependent:

$$f^{full}(\vec{q}, \hbar\omega) = f(\vec{q}) + f'(\hbar\omega) + i f''(\hbar\omega), \quad (2.3)$$

where $\hbar\omega$ is the photon energy. $f'(\hbar\omega)$ accounts for ways that electrons with different binding energies respond to the incoming field, and the term $i f''(\hbar\omega)$ arises from the binding energy which acts as a damping mechanism to the otherwise free electron density. The calculated values of the energy dependent terms for single atoms are tabulated [19]. These terms are relevant when doing REXS, where the quantum mechanical description is needed.

X-ray scattering in the solid state can benefit from the fact that the atoms are arranged in a periodic lattice. In doing so, each atom constitutes a scattering entity (as described above), but the contribution of each atom must be summed discretely, which yields the crystal structure factor $F(\vec{q})$, given by

$$F(\vec{q}) = \sum_{\vec{R}} f(\vec{q}) e^{i\vec{q} \cdot \vec{R}}; \vec{R} = n_1 \vec{a}_1 + n_2 \vec{a}_2 + n_3 \vec{a}_3 \quad (2.4)$$

where \vec{R} represents the position of an ion. The scattered intensity, $|F|^2$, takes on a large value when all the scattered waves scatter in phase. This condition is met if the scattering vector is such that $\vec{q} \cdot \vec{R} = 2\pi m$, where m is any integer, defining the **reciprocal lattice**, expressed as

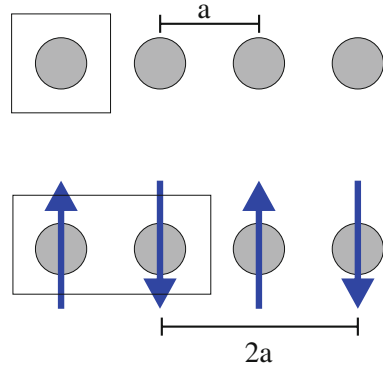
$$\vec{a}_i^* = 2\pi \frac{\vec{a}_j \times \vec{a}_k}{\vec{a}_1 \cdot (\vec{a}_2 \times \vec{a}_3)} = 2\pi \frac{\vec{a}_j \times \vec{a}_k}{V}, \quad (2.5)$$

where the i, j, k -indices follow cyclic notation, V is the volume of the unit cell (from the scalar triple product). These reciprocal lattice vectors, defined as $\vec{G} = h\vec{a}_1^* + k\vec{a}_2^* + l\vec{a}_3^*$, where h, k, l are integers, also have a periodicity and thus a fundamental ‘unit cell’, known as the Brillouin zone. Therefore, Fourier-transforming the reciprocal lattice, measurable through diffraction, will yield the real space lattice. In more complex systems with multiple ions in the real space unit cell, the structure factor becomes

$$F(\vec{q}, E) = \sum_{\vec{r}_j} f^{full}(\vec{q}, E) e^{i\vec{q} \cdot \vec{r}_j} \sum_{\vec{R}_n} e^{i\vec{q} \cdot \vec{R}_n}, \quad (2.6)$$

where J is the number of distinct atoms in the unit cell and N is all the unit cells in the crystal. In an ideally perfect scenario, N growing to infinity will render $F(\vec{q})$ a Dirac delta function. In general, the maxima repeat every time $\vec{q} = \vec{G}$, although different crystal systems may render combinations of h, k, l -values which suppress the term

Fig. 2.5 When a chain of ions with lattice spacing a (upper panel) enters a AFM phase, the unit cell (area enclosed by a square) doubles (lower panel), which results in reciprocal space folded into half



$e^{i\vec{q}\cdot\vec{R}_n}$. These “selection rules” are very useful in non-resonant X-ray scattering, i.e. serve to identify the crystal symmetry. However, Templeton and Templeton [9] as well as Finkelstein et al. [20] first observed forbidden reflections appearing close to resonance. This spawned the notion that anisotropic crystals can distort the electronic wave function, and the form factor takes on a highly non-trivial matrix form when approaching the resonant condition. In general, the form of $f^{full}(\vec{q}, \hbar\omega)$ in Eq. 2.3 describes the essence of REXS. In the following sections, specific aspects of this form factor will be derived.

Finally, ordering phenomena in crystals can change the lattice periodicity and be detected by diffraction. A crystal with a real space lattice defined in Eq. 2.6 will yield diffraction peaks when $\vec{q} = \vec{Q}$, i.e. integer values of h, k, l governed by their selection rules. In general, however, an ordered state of any kind (charge, spin, orbital) might change the symmetry of the crystal, and thus call for a new lattice definition. For example, take a simple 1-dimensional system of non-magnetic ions, whose period is defined as a , so $Q = 2\pi/a$. If the system were to take on AFM order, this will yield a new unit cell double in size to the original, setting $a' = 2a$ and $Q' = \pi/a$. In this case, the Brillouin zone defined before will reduce into half. This is shown in Fig. 2.5, which can easily be extended to 3-dimensions. However, instead of redefining the set of reciprocal lattice vectors \vec{Q}' , non-integer (h, k, l) -values are commonly used within the preceding reciprocal lattice definition \vec{Q} . For general ordered state, where different periodicities can be induced in all three crystallographic directions, the labeling $(\frac{h}{n_1}, \frac{k}{n_2}, \frac{l}{n_3})$ takes a frequent use, where the integers n_i refer to the manifold multiplication of the unit cell along the axis i . However, some ordered states can create charge and/or spin textures which are not commensurate with the crystal lattice. For such a case, not even a new definition of integer (h, k, l) -values would yield a simple description of the system. Therefore, the use of $(\frac{h}{n_1}, \frac{k}{n_2}, \frac{l}{n_3})$, with non-integer n_i , is required. These kinds of order are known as *incommensurate*, and we will see a manifestation of it in Chap. 4.

2.3.2 The Interaction of Light with Matter

In general, light and matter interactions serve a very important tool in condensed matter research. A medium exposed to an external electromagnetic wave will drive the system out of equilibrium through the duration of the interaction. Some properties of the system will couple to the external field and thus be altered in a specific way. For the case of low excitation fields, the change that the external field exerts on the system is proportional to that field, and this proportionality constant is known as the linear response function. Examples in other fields of such a function are specific heat, magnetic susceptibility, compressibility, etc. This section will describe the process of XAS and elastic scattering within the framework of linear response theory. In other words, a system's reaction to an X-ray perturbation can be used to extract information about it. This will lead to an expression which corresponds to $f^{full}(\vec{q}, E)$ in Eq. 2.3.

Consider an oscillating electron perturbed by an time-dependent external field. The Hamiltonian for such a scenario looks like $H = H_0 + H_{ext}$, where H_0 is the unperturbed, equilibrium state, and H_{ext} is the perturbation field, in this case the electromagnetic wave $\equiv \vec{E}_{in}$. For small perturbations H_{ext} , as is the case in most particle scattering experiments, the polarization vector of the electron responds linearly to the field:

$$\vec{P} = \chi \vec{E}_{in}(t), \quad (2.7)$$

where χ is defined as the electric susceptibility of the electron, a quantity describing how easily the system can be polarized. For an electromagnetic wavefield, $\vec{E}_{in}(t) = \hat{e} E_0 e^{-i(\omega t - \vec{k} \cdot \vec{r})}$, where \hat{e} is a unit vector along the polarization of the wave which is complex (circular light), E_0 is the amplitude of the field, and ω its frequency. The velocity and acceleration of the electron are:

$$\vec{j} \equiv \frac{\partial \vec{P}}{\partial t} = -i\omega\chi \vec{E}_{in}(t) \quad (2.8)$$

and

$$\vec{a} \equiv \frac{\partial \vec{j}}{\partial t} = \omega^2 \chi \vec{E}_{in}(t) \quad (2.9)$$

where the latter quantity implies a radiated field, i.e. $\vec{a} \propto \vec{E}_{out}$. The absorption process can be viewed as the damping of the oscillatory motion of the electron as it dissipates energy from $\vec{E}_{in}(t)$. This is equal to the power it absorbs, which is given by the time-averaged work done by the oscillator:

$$W = \frac{1}{T} \int_0^T \vec{F} \cdot \vec{j} dt = \langle \vec{E}_{in} \cdot \vec{j} \rangle = \frac{1}{2} \text{Re}[\vec{E}_{in}^* \cdot (-i\omega\chi) \vec{E}_{in}], \quad (2.10)$$

where the later step involves simple complex number algebra. Introducing the conductivity $\sigma(\hbar\omega) = \omega\chi$, we obtain a simple expression for the absorption process:

$$I_{XAS}(\hbar\omega) = \frac{1}{2} \text{Im}[\hat{\epsilon}^* \cdot \sigma(\hbar\omega) \cdot \hat{\epsilon}]. \quad (2.11)$$

We note at this point, that σ is not necessarily a scalar quantity, so generally it is referred to as the *conductivity tensor*. It has a real and imaginary part, which arise from the solution to the differential equation of a damped oscillator. Thus, it follows that these two components of σ are Kramers-Kronig related.³ Therefore, this quantity can be connected to the term $f^{full}(\vec{q}, E)$ in Eq. 2.3, as follows

$$\sigma(\hbar\omega) \propto f'(\hbar\omega) + if''(\hbar\omega), \quad (2.12)$$

which directly links the conventional notion that $f''(\hbar\omega)$ is related to the XAS process.

Detecting a scattering process, moreover, is a quantification of the radiated field of the accelerated electron. It is the squared norm of the radiated field divided by the squared norm of the incoming field. Using the definitions above, this comes down to

$$I_{REXS}(\hbar\omega) = \frac{|\vec{E}_{out}|^2}{|\vec{E}_{in}|^2} \propto |\hat{\epsilon}_{out}^* \cdot \sigma \cdot \hat{\epsilon}_{in}|^2. \quad (2.13)$$

Equations 2.12 and 2.13 reveal that the conductivity tensor σ holds the pertinent information about the system, showing the connection between absorption and scattering of X-rays in analogy to the optical description.

2.3.3 XAS Cross Section

The development of the XAS cross section begins with quantum mechanical, first-order perturbation theory. In this case, the system is described by a time-dependent Hamiltonian $H = H_0 + H_{ext}$. The term H_0 refers to the unperturbed system, in this case the ion or cluster to consider, with eigenstates $H_0|\varphi_0\rangle = E_n|\varphi_0\rangle$, and H_{ext} arises from the potential field of the light, $\vec{A}(\vec{r}, t)$, and the canonical transformation of the momentum. The time-dependent part of the Hamiltonian is H_{ext} . For a light-matter interaction, the full Hamiltonian contains the terms [21]:

$$\begin{aligned} H_1 &= \frac{e^2}{2m} \vec{A}^2 \\ H_2 &= -\frac{e}{mc} \vec{p} \cdot \vec{A} \\ H_3 &= -\frac{e\hbar}{mc} \vec{s} \cdot (\nabla \times \vec{A}) \end{aligned} \quad (2.14)$$

³ The connection between a damped oscillator and the Kramers-Kronig relations is given in Appendix 4.3.3.

$$H_4 = -\frac{e\hbar}{2m^2c^3}\vec{s}\left(\frac{\partial\vec{A}}{\partial t}\times\frac{e}{c}\vec{A}\right).$$

The term H_1 is responsible for so-called Thomson scattering, involves the field potential interacting with itself so it is left out of the REXS process. The term H_4 , on the other hand, is quadratic in \vec{A} and describes the non-resonant magnetic scattering process, which we will not discuss in this section. The terms H_2 and H_3 describe the resonant process, and thus their inspection is needed. The term H_3 is related to the spin, but the higher order terms of the Taylor expansion of the exponential (see below) can be regrouped with high-order multipole terms of H_2 and will thus not be considered further. We will see, moreover, how the magnetic terms can later be incorporated into σ . It is therefore from the term $H_{ext} = H_2$ that we will derive the connection between σ and the transition rate matrix. Also known as Fermi's Golden Rule, this matrix is an important quantity in experimental spectroscopy.

We begin by expressing the momentum operator $\vec{p} = im[H, \vec{r}]$, which can be derived from the canonical commutation relations. Thus, H_{ext} can be expressed as

$$H_{ext} = \frac{ie}{m^2}[H, \vec{r}] \cdot \vec{A}. \quad (2.15)$$

The photon field potential \vec{A} has the form of a traveling wave, i.e.

$$\vec{A} = A_0\hat{e}e^{-i(\omega t + \vec{k}\cdot\vec{r})} + A_0\hat{e}^*e^{i(\omega t + \vec{k}\cdot\vec{r})} = 2A_0\hat{e}\cos(\omega t + \vec{k}\cdot\vec{r}). \quad (2.16)$$

Using the gauge transformations $\vec{E} = -\frac{\partial\vec{A}}{\partial t}$, the last term can be expressed in terms of the electric field as $\vec{E} = 2i\omega A_0\hat{e}\sin(\omega t + \vec{k}\cdot\vec{r})$. So H_{ext} becomes

$$H_{ext} = \frac{eE_0}{2m^2\omega}[H, \vec{r}] \cdot \hat{e}e^{i\vec{k}\cdot\vec{r}}, \quad (2.17)$$

where $E_0 = 2i\omega A_0$.

Fermi's Golden Rule, on the other hand, is a way to calculate the rate of transition into a certain state, given a perturbation acting on the system. In other words,

$$I_{XAS} = \sum_f |\langle f|H_{ext}|i\rangle|^2 (\delta(\omega + E_i - E_f) + \delta(\omega - E_i + E_f)), \quad (2.18)$$

where the initial and final states of the transition are labeled i and f , and the delta functions appear to enforce energy conservation.⁴ Having a useful expression for H_{ext} , we turn to calculate the matrix element:

⁴ More details on the derivation of Fermi's Golden Rule can be found in Appendix 4.3.3.

$$\begin{aligned}
\langle f | H_{ext} | i \rangle &= \langle f | \frac{e}{2m^2\omega} [H, \vec{r}] \cdot \hat{\epsilon} e^{i\vec{k} \cdot \vec{r}} | i \rangle \\
&= \frac{eE_0}{2m^2\omega} (E_f - E_i) \langle f | \vec{r} \cdot \hat{\epsilon} e^{i\vec{k} \cdot \vec{r}} | i \rangle.
\end{aligned} \tag{2.19}$$

When the photon's energy matches the transition, $\omega \propto E_f - E_i$ we obtain an expression for I_{XAS} :

$$I_{XAS} = \frac{eE_0^2}{2m^2} \sum_f \langle f | \vec{r} \cdot \hat{\epsilon} e^{i\vec{k} \cdot \vec{r}} | i \rangle^2 (\delta(\omega + E_i - E_f) + \delta(\omega - E_i + E_f)). \tag{2.20}$$

In real physical experiments, Dirac functions are replaced by Lorentzian functions, which can be done mathematically through the transformation

$$\delta(x) = -Im(\lim_{\Gamma \rightarrow 0} \frac{1}{\pi(x + i\Gamma/2)}), \tag{2.21}$$

where Γ is the width. Developing an expression for I_{XAS} :

$$\begin{aligned}
I_{XAS} &= \frac{eE_0^2}{2m^2} \sum_f |\langle f | \vec{r} \cdot \hat{\epsilon} e^{i\vec{k} \cdot \vec{r}} | i \rangle|^2 (\delta(\omega + E_i - E_f)) \\
&= -\frac{eE_0^2}{2m^2} Im \sum_f (\lim_{\Gamma \rightarrow 0} |\langle f | \vec{r} \cdot \hat{\epsilon} e^{i\vec{k} \cdot \vec{r}} | i \rangle|^2 \frac{1}{\pi(\omega + E_i - E_f + i\Gamma/2)} \\
&\quad + \frac{1}{\pi(\omega - E_i + E_f + i\Gamma/2)}) \\
&= -\frac{eE_0^2}{2m^2} Im \sum_f \lim_{\Gamma \rightarrow 0} \langle i | (\vec{r} \cdot \hat{\epsilon} e^{i\vec{k} \cdot \vec{r}})^\dagger | f \rangle (\frac{1}{\pi(\omega + E_i - E_f + i\Gamma/2)} \\
&\quad + \frac{1}{\pi(\omega - E_i + E_f + i\Gamma/2)}) \langle f | (\vec{r} \cdot \hat{\epsilon} e^{i\vec{k} \cdot \vec{r}}) | i \rangle \\
&= -\frac{eE_0^2}{2m^2} Im \lim_{\Gamma \rightarrow 0} \langle i | (\vec{r} \cdot \hat{\epsilon} e^{i\vec{k} \cdot \vec{r}})^\dagger (\frac{1}{\pi(\omega + E_i - H + i\Gamma/2)} \\
&\quad + \frac{1}{\pi(\omega - E_i + H + i\Gamma/2)}) (\vec{r} \cdot \hat{\epsilon} e^{i\vec{k} \cdot \vec{r}}) | i \rangle.
\end{aligned} \tag{2.23}$$

Using the Taylor expansion of the exponential, the first approximation simplifies $H_{ext} \rightarrow \hat{\epsilon} \cdot \vec{r}$, yielding the dipole approximation (E1) which is useful to model most scattering processes. Mentioned for completeness, the linear term of the expansion is the so-called quadrupole term (E2), with an interaction Hamiltonian that looks like $\hat{\epsilon} \cdot \vec{k} \vec{r} \cdot \vec{r}$.

Finally, comparing Eqs. 2.11 and 2.22, a useful expression for σ can be written as

$$\sigma = \frac{e}{2\pi m^2} \langle i | \vec{r} \left(\frac{1}{\omega + E_i - H + i\Gamma/2} + \frac{1}{\omega - E_i + H + i\Gamma/2} \right) \vec{r} | i \rangle. \quad (2.24)$$

The process can be described as follows: the Hamiltonian H acts twice on the system, driving the system into an intermediate state, also known as the core-hole state, and returning it to its initial state. Thus, knowing the eigenvalues of the Hamiltonian H in the core-hole state will suffice to calculate the conductivity tensor σ , and all the cross sections needed for scattering experiments. The resonant enhancement to the scattered intensity is evident from the divergence of the denominators with photon energies tuned to the right transitions. In practice, for $3d$ TMOs, $L_{2,3}$ -edge enhancements can reach up to several orders of magnitude.

Finally, we turn to derive rules for the transition to take place with non-zero probability. For this purpose, we make use of the spherical harmonic expression of the wave functions and the photon field. Consider the case of linear polarization along \vec{z} , the dipole term can be expressed as $r \cos(\theta) \propto r Y_0^1(\theta, \phi)$. The case for circular polarization is $\propto r Y_{\pm 1}^1(\theta, \phi)$, indicating that the angular part of the integral $\langle l' m' | Y_m^1(\theta, \phi) | l m \rangle$ will yield selection rules for the transition process. For linear polarized light, the rules are $\Delta l = \pm 1$ and $\Delta m = 0, \pm 1$.

The studies presented in this thesis involve $L_{2,3}$ -edges of $3d$ TMOs. In this case, the transition corresponds to $2p \rightarrow 3d$. Since the electronic states of interest, close to the Fermi level, are around the $3d$ -level, this transition is the key one to investigate these systems. Furthermore, spin-orbit coupling splits the $2p$ core-hole state into two: $2p_{3/2}$ and $2p_{1/2}$. These states are separated by ~ 10 eV for these systems. This yields two available transitions, which are usually called L_3 ($2p_{3/2} \rightarrow 3d$) and L_2 ($2p_{1/2} \rightarrow 3d$). The final state $3d$, moreover, also has several features which can be probed using X-rays. The real-space orbitals that were outlined in Chap. 1, t_{2g} and e_g , and their occupation number are useful quantities that we will discuss later. A schematic of a transition of electrons into the $3d$ shell is shown in Fig. 2.6, which illustrates a process that represents the fundamental backbone of resonant X-ray physics in TMOs.

2.3.3.1 A Two Level System

We proceed to calculate the conductivity tensor σ for the simple case of a system with two levels, which also serves a realistic approach because REXS experiments are taken in the vicinity of one absorption edge, i.e. one transition element. We take a transition $|s\rangle \rightarrow |p\rangle$, and we define the difference in energy between the two states as ω_0 . In that case, we can evaluate the expression 2.24, and obtain

$$\sigma = \frac{e}{2\pi m^2} \left(\frac{1}{\omega + \omega_0 + i\Gamma/2} + \frac{1}{\omega - \omega_0 + i\Gamma/2} \right). \quad (2.25)$$

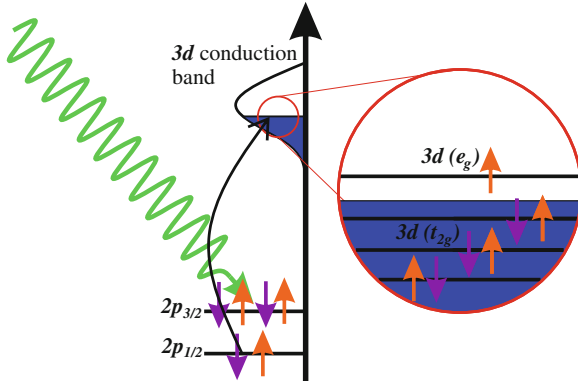


Fig. 2.6 A schematic of a photon inducing a $2p \rightarrow 3d$ transition. This example portrays a $3d^7$ system with crystal field separating the t_{2g} and e_g into a low spin state

Fig. 2.7 A plot of the real and imaginary part of σ , taking $\omega_0 = 854$ eV, and the broadening $\Gamma = 0.5$ eV

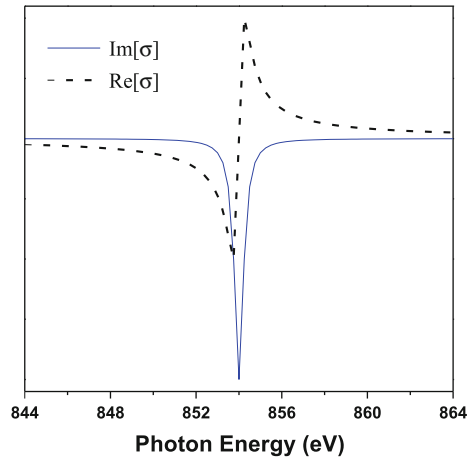


Figure 2.7 shows the resulting projections of σ on the imaginary and real axes, taking the values of ω_0 and Γ listed in the caption, which resemble the Kramers-Kronig related response of the damped oscillator.

Furthermore, the tensor character of σ can generally be expressed in matrix form as follows:

$$\sigma(\omega) = \begin{pmatrix} \sigma_{xx} & \sigma_{xy} & \sigma_{xz} \\ \sigma_{yx} & \sigma_{yy} & \sigma_{yz} \\ \sigma_{zx} & \sigma_{zy} & \sigma_{zz} \end{pmatrix}. \quad (2.26)$$

In this general case, the symmetry of the final state will be represented in the (in)equivalency of the terms σ_{ij} . For example, a final state with $|p\rangle$ -character will yield a matrix of the form

$$\sigma_{s \rightarrow p}(\omega) = \begin{pmatrix} \sigma_{s \rightarrow p_x} & \sigma_{s \rightarrow p_{xy}} & \sigma_{s \rightarrow p_{xz}} \\ \sigma_{s \rightarrow p_{yx}} & \sigma_{s \rightarrow p_y} & \sigma_{s \rightarrow p_{yz}} \\ \sigma_{s \rightarrow p_{zx}} & \sigma_{s \rightarrow p_{zy}} & \sigma_{s \rightarrow p_z} \end{pmatrix}.$$

where off-diagonal elements will be projections of the $|p_{x,y,z}\rangle$ states off the cartesian axes. Consider, a $|p\rangle$ -state in cubic symmetry, where $|p_x\rangle \equiv |p_y\rangle \equiv |p_z\rangle$, then the terms σ_{ii} are all equal, and the off-diagonal $\sigma_{ij} = 0$. For the case of tetragonal symmetry, which is one commonly considered in TMO heterostructures, epitaxial strain usually distorts the lattice in-plane. This might introduce an energy separation between otherwise degenerate orbitals (like p or d), and so the conductivity tensor becomes,

$$\sigma^{tetragonal}(\omega) = \begin{pmatrix} \sigma_{xx} & 0 & 0 \\ 0 & \sigma_{xx} & 0 \\ 0 & 0 & \sigma_{zz} \end{pmatrix}.$$

Recalling Eq. 2.11, taking the coordinates of the light polarization in the linear, cartesian basis, a conductivity tensor of this form will yield inequivalent spectra when the polarization of the incoming light is in- or out-of-plane. This phenomenon, called natural linear dichroism (LDIC), can be very useful to determine the occupation of non-degenerate e_g orbitals, as can be visualized in Fig. 2.8. In that case, depicting a typical measurement geometry available in heterostructures grown on a tetragonal substrate, the light with polarization in-plane (\hat{e}_{ab}) will couple with the terms σ_{xx} . Similarly, the light with perpendicular linear polarization will have a component on the c axis, so \hat{e}_c can couple into the states σ_{zz} . In $3d$ systems like the ones investigated in this thesis, the character of σ_{xx} and σ_{zz} can be directly related to the occupation of the e_g orbitals. A prime example of an application of such linear dichroism in TMO heterostructures can be found in Refs. [22–25]. Later, we will see how this plays a role in the magnetic properties of RNO heterostructures. We note that other crystal symmetries result in different relations between σ_{ij} , with the triclinic system with lowest symmetry rendering 6 unequal matrix elements (3 different diagonal elements, and 3 more obeying the condition $\sigma_{ij} = \sigma_{ji}$).

In summary, we derived and discussed the importance of the scattering tensor σ , which contains the information about the system under investigation. It holds the key for the interpretation of XAS, especially when considering symmetries which can manifest in dichroism effects. Because of the relation between σ and the scattered signal given by Eq. 2.13, these symmetry details will reappear, and sometimes more effectively, in the scattered signal. Equation 2.26 shows the general form of the conductivity tensor.

Finally, to lead in to the following section, we briefly discuss the basic form of a magnetic conductivity tensor. Consider a cubic system with a net magnetization along the \hat{z} -direction. Classically, the magnetic field will create a Lorentz force which creates a Hall current in the xy -plane, modifying the electric permittivity into $\vec{D} = \hat{\epsilon} \vec{E} = \hat{\epsilon}' \vec{E} + i \vec{g} \times \vec{E}$, where \vec{g} is the gyromagnetic ratio. This results in the well-known off-diagonal, imaginary terms in σ , which lead to the magneto optical phenomena like the Kerr and Faraday effect. Quantum mechanically, spin-orbit coupling and

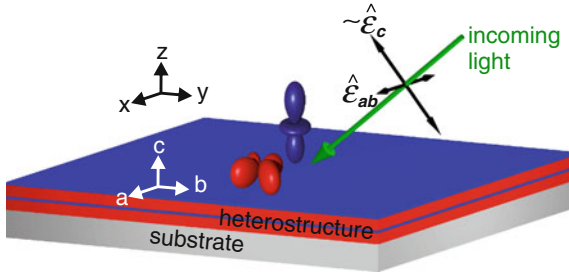


Fig. 2.8 A schematic of a LD experiment of a heretostructure grown on a substrate. The polarization vectors are either in-plane ($\hat{\epsilon}_{ab}$) or have a component out-of-plane ($\hat{\epsilon}_c$). The former couples into states with $x^2 - y^2$ symmetry (*red orbitals*), and the latter to $3z^2 - r^2$ states (*purple orbitals*). Thus, this measurement can probe the unbalance of occupation of such states

time-reversal symmetry breaking causes the tensor to take on imaginary off-diagonal elements. The cubic system described above results in a tensor like

$$\sigma_z^{\text{magnetic}}(\omega) = \begin{pmatrix} \sigma_{xx} & i\sigma_{xy} & 0 \\ -i\sigma_{xy} & \sigma_{xx} & 0 \\ 0 & 0 & \sigma_{zz} \end{pmatrix}.$$

2.3.4 Magnetic Scattering: Symmetry Considerations

We now turn to discuss in more detail the different forms that σ can take in the presence of a magnetic moment, and the implications it has in the scattered signal. This will provide the tools needed for magnetic structure determination using RSXS. The majority of this section's scope was obtained from Refs. [10, 12, 16] and others therein.

We begin by considering the general form of the scattering tensor in for any crystal symmetry to consider:

$$F(\omega) = \begin{pmatrix} F_{xx}(\omega) & F_{xy}(\omega) & F_{xz}(\omega) \\ F_{yx}(\omega) & F_{yy}(\omega) & F_{yz}(\omega) \\ F_{zx}(\omega) & F_{zy}(\omega) & F_{zz}(\omega) \end{pmatrix},$$

where we make use of Cartesian coordinates highlighting that even in the presence of a randomly oriented magnetic moment, the strong energy dependence of $F(\omega)$ can be projected to the principal axes which are in turn aligned with the crystal axes. Note that taking high crystal symmetries and its set of symmetry operations Γ without a moment will simplify the form of $F(\omega)$. Furthermore, consider now the presence of a magnetic moment along a random orientation. It is easy to visualize that any operation Γ will break the symmetry by inevitably rotating the moment,

leaving only the identity operation as valid. Thus, a new symmetry operation Γ' will require first a rotation of the whole system, Γ , and then a rotation of the magnetic moment back. That is, we will treat the moment and the system it lies in separately, defining $F(\omega) \equiv F_1(\omega, \hat{e})F_2(\vec{M})$, where one part depends only on the energy and polarization of the light and the other term holds the magnetic moment's identity. This can be achieved by expanding the terms of $F(\omega)$ in spherical harmonics on the unit sphere, that is

$$F(\theta, \phi, \omega) = \sum_{k=0}^{\infty} \sum_{m=-k}^k \begin{pmatrix} F_{xx}^{km}(\omega) & F_{xy}^{km}(\omega) & F_{xz}^{km}(\omega) \\ F_{yx}^{km}(\omega) & F_{yy}^{km}(\omega) & F_{yz}^{km}(\omega) \\ F_{zx}^{km}(\omega) & F_{zy}^{km}(\omega) & F_{zz}^{km}(\omega) \end{pmatrix} Y_{km}(\theta, \phi), \quad (2.27)$$

where θ, ϕ define the moment's direction in spherical coordinates from

$$\vec{M} = \begin{pmatrix} m_x \\ m_y \\ m_z \end{pmatrix} = \begin{pmatrix} |\vec{M}| \cos(\phi) \sin(\theta) \\ |\vec{M}| \sin(\phi) \sin(\theta) \\ |\vec{M}| \cos(\theta) \end{pmatrix},$$

and Y_{km} are the spherical harmonics. The $F_{ij}(\omega)$'s are the components of the scattering tensor on the basis of linear polarized light projected on the crystal system, that is $\hat{e} \equiv (\epsilon_x, \epsilon_y, \epsilon_z)$. Now, to calculate the set of allowed coefficients of the expansion, the same set of symmetry operations considerations will be taken, that is $\Gamma'F = F$. In other words, $F(\omega)$ must fulfill the symmetry of the system. The simplest operation to consider is a 4-fold rotation along the z -axis ($C_4(z)$), which implies rotating the system and the magnetic moment by $-\pi/2$, and then rotating $F(\omega)$ back:

$$\begin{aligned} & \begin{pmatrix} 0 & 1 & 0 \\ -1 & 0 & 0 \\ 0 & 0 & 1 \end{pmatrix} \cdot \sum_{k=0}^{\infty} \sum_{m=-k}^k \begin{pmatrix} F_{xx}^{km} & F_{xy}^{km} & F_{xz}^{km} \\ F_{yx}^{km} & F_{yy}^{km} & F_{yz}^{km} \\ F_{zx}^{km} & F_{zy}^{km} & F_{zz}^{km} \end{pmatrix} Y_{km}(\theta, \phi) \cdot \begin{pmatrix} 0 & -1 & 0 \\ 1 & 0 & 0 \\ 0 & 0 & 1 \end{pmatrix} \\ &= \sum_{k=0}^{\infty} \sum_{m=-k}^k \begin{pmatrix} F_{yy}^{km} & -F_{yx}^{km} & F_{yz}^{km} \\ -F_{xy}^{km} & F_{xx}^{km} & -F_{xz}^{km} \\ F_{zy}^{km} & -F_{zx}^{km} & F_{zz}^{km} \end{pmatrix} Y_{km}(\theta, \phi - \pi/2), \end{aligned}$$

which gives a set of rules to evaluate the coefficients F_{ij} .

The first, simplest, and perhaps most useful system to consider is the case of spherical symmetry. In this case, the ϕ -dependent part of the function can be integrated out, and the properties of the remaining Legendre polynomials ($\int P_m(\cos \theta) d \cos \theta = 0$ unless $m = 0$) reduce the summation over m to one term. In addition, following the triangular truncation procedure, the summation on k is only taken for $k \in \{0, 1, 2\}$. So we can easily see the rules the coefficients must follow:

$$\sum_{k=0}^2 F_{yx}^{k0} Y_{k0}(\theta, \phi) = - \sum_{k=0}^2 F_{xy}^{k0} Y_{k0}(\theta, \phi - \pi/2),$$

$$\begin{aligned}\sum_{k=0}^2 F_{zz}^{k0} Y_{k0}(\theta, \phi) &= \sum_{k=0}^2 F_{zz}^{k0} Y_{k0}(\theta, \phi - \pi/2), \\ \sum_{k=0}^2 F_{xx}^{k0} Y_{k0}(\theta, \phi) &= \sum_{k=0}^2 F_{yy}^{k0} Y_{k0}(\theta, \phi - \pi/2),\end{aligned}$$

and all other coefficients are 0. After some algebra, we arrive at the expression for a magnetic moment along the \vec{z} -direction, i.e. setting $\theta = \pi/2$:

$$F_{\vec{z}}^{mag} = \begin{pmatrix} F^{(0)} - \frac{1}{3}F^{(2)} & -F^{(1)} & 0 \\ F^{(1)} & F^{(0)} - \frac{1}{3}F^{(2)} & 0 \\ 0 & 0 & F^{(0)} + \frac{2}{3}F^{(2)} \end{pmatrix}. \quad (2.28)$$

More realistic scenarios, however, will not have the magnetic moment along such a high symmetry direction. Indeed determining the direction of the moment is a problem that REXS is viable to address. For that reason, we turn to develop an expression for F^{mag} with a random orientation. This is done simply by taking the tensor $F_{\vec{z}}^{mag}$ and rotating it to a random direction: $F^{mag} = R F_{\vec{z}}^{mag} R^T$, where the rotation matrix defining the spherical angles (ϕ, θ) is given by

$$R = \begin{pmatrix} \cos(\phi) & -\sin(\phi) & 0 \\ \sin(\phi) & \cos(\phi) & 0 \\ 0 & 0 & 1 \end{pmatrix} \cdot \begin{pmatrix} \cos(\theta) & 0 & \sin(\theta) \\ 0 & 1 & 0 \\ -\sin(\theta) & 0 & \cos(\theta) \end{pmatrix}.$$

This yields the general form of F^{mag} in spherical symmetry:

$$F^{mag} = \begin{pmatrix} F^{(0)} + (x^2 - \frac{1}{3})F^{(2)} & -zF^{(1)} + xyF^{(2)} & yF^{(1)} + xzF^{(2)} \\ zF^{(1)} + xyF^{(2)} & F^{(0)} + (y^2 - \frac{1}{3})F^{(2)} & -xF^{(1)} + yzF^{(2)} \\ -yF^{(1)} + xzF^{(2)} & xF^{(1)} + yzF^{(2)} & F^{(0)} + (z^2 - \frac{1}{3})F^{(2)} \end{pmatrix}. \quad (2.29)$$

In magnetic diffraction experiments, the quantity I_{REXS} of Eq. 2.13 must contain the phase shift of the diffracted wave. In other words

$$I_{mag} = \left| \sum_i e^{i(\vec{k}_{in} - \vec{k}_{out}) \cdot \vec{r}_i} \hat{\epsilon}_{out}^* \cdot F_i^{mag} \cdot \hat{\epsilon}_{in} \right|^2, \quad (2.30)$$

where $\hat{\epsilon}_{in,out}$ represent the polarization vectors of in- and out-coming light, and likewise $\vec{k}_{in,out}$ represent the wave vectors of both light states, which are set by the requirement of fulfilling the Bragg condition. \vec{r}_i , F_i^{mag} represent the position and scattering tensor of the i -ion, and the summation runs over the sample size, but the phase information is entirely encoded by running the summation over the magnetic unit cell. In a practical experiment, the polarization vectors can be tuned using the parameters of the undulator (Sect. 2.2) between circular left and right, and linear vertical and horizontal. The latter two define the most useful set of coordinates as

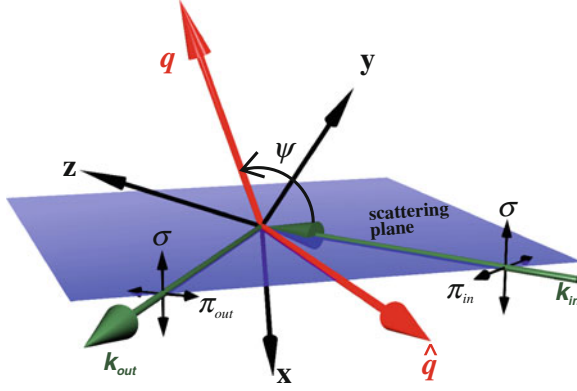


Fig. 2.9 The definition of the vectors used in the description of the scattering process in the main text, combining the visualization in the crystal frame and in the experimental scattering frame. The crystal axes lie in an arbitrary position, determined by the position in q -space where the Bragg peak of interest lies. The figure does not show the direction of the magnetic moment, which will be determined later

follows. Let π be the linear polarization state parallel to the scattering plane, and σ the one perpendicular, as in Fig. 2.9.⁵

We express now the light wave propagation vectors $\vec{k}_{in,out}$ in the cartesian coordinate system we have defined. Let $\hat{q} \equiv \{q_x, q_y, q_z\}/|\vec{q}|$, and \hat{q}_\perp any vector perpendicular to it, which will be needed to define the scattering plane in these coordinates. Now, let ψ be the angle between \hat{q}_\perp and the scattering plane. The angle between \vec{k}_{in} and \hat{q} , related to the Bragg angle, we call θ . So now we can define all the needed vectors in the crystal coordinates, as follows:

$$\begin{aligned}
 \vec{k}_{in} &\parallel \sin(\theta)[\cos(\psi)\hat{q}_\perp + \sin(\psi)(\hat{q}_\perp \times \hat{q})] + \cos(\theta)\hat{q}, \\
 \vec{k}_{out} &\parallel \sin(\theta)[\cos(\psi)\hat{q}_\perp + \sin(\psi)(\hat{q}_\perp \times \hat{q})] - \cos(\theta)\hat{q}, \\
 \sigma_{in} = \sigma_{out} &\equiv \sigma = (\vec{k}_{in} \times \vec{k}_{out})/\sin(2\theta), \\
 \pi_{in} &= (\vec{k}_{in} \times \sigma), \\
 \pi_{out} &= (\vec{k}_{out} \times \sigma).
 \end{aligned} \tag{2.31}$$

Finally, the polarization vectors $\hat{e}_{in,out}$ can be written as linear combinations of the vectors σ and π . So now we define the four experimental quantities that can, in principle, be measured in experiment at a fixed angle: F_{ij} , where $ij \in \{\sigma, \pi\}$. For example, one of the four channels can be $F_{\sigma\sigma} \equiv (\sigma \cdot F \cdot \sigma)$, so the four channels are $F_{\sigma\pi}, F_{\sigma\sigma}, F_{\pi\sigma}, F_{\pi\pi}$. Completely discerning the polarization state of the outgoing light is possible using a polarization analyzer of the scattered beam, which is not always available, especially in the soft X-ray regime. However, measuring four linear-independent spectra ($\sigma, \pi, \sigma + \pi, \sigma + i\pi$, the latter two being linear 45° rotated

⁵ Not to be confused with the conductivity tensor σ , shown in non-bold typeface in this work.

and circular light) yields enough information to map out the scattering tensor on the basis of σ, π . In many cases, enough information about the scattering tensor can be obtained by measuring only the two states σ, π , provided the azimuthal dependence can be measured. Then, the two measurable channels are given by

$$\mathbf{I}_\pi = I_{\pi\sigma} + I_{\pi\pi}; \mathbf{I}_\sigma = I_{\pi\sigma}, \quad (2.32)$$

where we will show later how the channel $I_{\sigma\sigma}$ goes to 0. Finally, we turn to express F^{mag} in terms of the experimentally accessible vectors $\hat{\epsilon}_{in,out}$, evaluating the expression 2.29 and carrying out some algebra leads to:

$$F^{mag} = F^{(0)}(\hat{\epsilon}_{out}^* \cdot \hat{\epsilon}_{in}) + F^{(1)}(\hat{\epsilon}_{in} \times \hat{\epsilon}_{out}^*) \cdot \hat{m} + F^{(2)}(\hat{\epsilon}_{out}^* \cdot \hat{m})(\hat{\epsilon}_{in} \cdot \hat{m}), \quad (2.33)$$

which is the result obtained by Hannon et al. [10], a long-standing and widely used expression for magnetic scattering in spherical symmetry. Note that in their approach, the magnetic Hamiltonian, H_3 in Eq. 2.14, was the starting point to calculate the scattered intensity. In the approach described here, the magnetic moment information is contained in the scattering tensor we have defined. From Eq. 2.33, it can now be seen which terms will be needed to interpret the scattered intensity of a AFM system. $F^{(0)}$ has no term proportional to the magnetic moment and is usually disregarded in magnetic scattering. The term $F^{(1)}$ is linear in \hat{m} and will give rise to the first harmonic of an AFM. This term is indeed related to the magnetic circular dichroism ($\Delta m_j = \pm 1$). The term proportional $F^{(2)}$ also has magnetic influence, but it is quadratic in \hat{m} , so it will be blind to an AFM system, canceling the antiparallel spin directions. If the AFM system is a spiral, then it will give rise to second harmonics, which require twice the momentum transfer to access the corresponding Bragg peak. A quintessential example of such a spiral system was studied in films of Holmium metal [26] and in manganites [27]. A visualization of this consequence can be seen in Fig. 2.10.

Therefore, the intensity of magnetic scattering is proportional to the terms containing $F^{(1)}$, which can be expressed in spherical symmetry as:

$$F^{mag} = \begin{pmatrix} 0 & -m_z & m_y \\ m_z & 0 & -m_x \\ -m_y & m_x & 0 \end{pmatrix}. \quad (2.34)$$

From this expression, it can be seen that for any vector \vec{v} , $\vec{v} \cdot F^{mag} \cdot \vec{v} = 0$. Therefore, knowing that vector σ remains unchanged during the scattering event (from Eq. 2.31 and Fig. 2.9), $F_{\sigma\sigma} = 0$ for resonant magnetic scattering. This expression also yields a valuable piece of information: the components of the magnetization direction m_i are encoded in the tensor F^{mag} , and they can be determined by measuring azimuthal scans around the Bragg condition \hat{q} , as shown in Fig. 2.11. For simplicity, the figure is represented in the laboratory frame of reference, as opposed to Fig. 2.9 which is in the crystal frame. Both are equivalent and advantageous depending on the discussion. In this thesis, the latter will be used, and we can arrive at expressions of the diffracted

Fig. 2.10 In a spiral, the term quadratic in \vec{m} will give rise to second harmonics of the first Bragg peak, which are double in momentum transfer

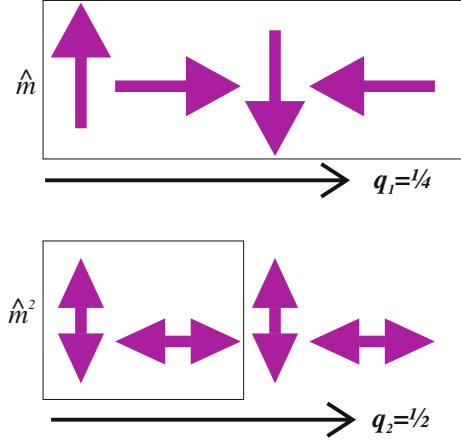
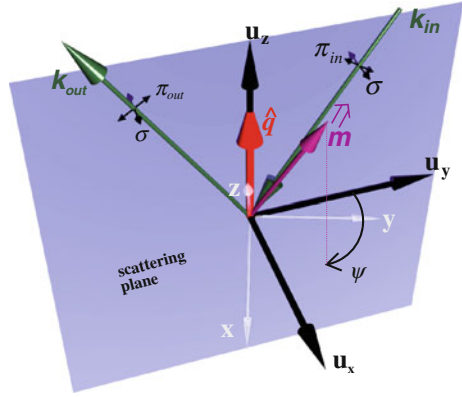


Fig. 2.11 The way the direction of a magnetic moment \vec{m} can be determined by doing azimuthal scans around the diffraction vector \hat{q} . Axes in this figure are defined in the laboratory reference frame, where the direction of the crystal axes (x, y, z) can be rather skew



intensity as a function of the azimuthal angle. For example, the channel $F_{\sigma\pi}$ for a simple AFM system looks like:

$$F_{\sigma\pi} = (\vec{k}_{out} \times \sigma) \left(e^{i0} \begin{pmatrix} 0 & -m_z & m_y \\ m_z & 0 & -m_x \\ -m_y & m_x & 0 \end{pmatrix} + e^{i\pi} \begin{pmatrix} 0 & m_z & -m_y \\ -m_z & 0 & m_x \\ m_y & -m_x & 0 \end{pmatrix} \right) (\vec{k}_{in} \times \vec{k}_{out}) / \sin(2\theta), \quad (2.35)$$

where the phase of $\vec{q} = \frac{1}{2}$ was taken, and the sum runs over two sites. Note that the second matrix in F represents a spin oriented antiparallel to the first. The terms $\vec{k}_{in,out}$ and σ contain the geometry information, including the azimuthal angle ψ . It is important to define here the reference frame, that is $\psi = 0^\circ$ and the sense of rotation. This is achieved by carefully defining \hat{q}_\perp at the value of $\psi = 0^\circ$, while the rotation around \hat{q} is defined as right handed.

Finally, for completeness, it is noted that the form of F^{mag} can change when considering systems beyond spherical symmetry. Although that was not the case during this thesis, there are systems which deviate substantially from spherical symmetry, and their scattering tensor must be considered accordingly. In our treatment, the different symmetries will arise from carrying out the summation over the spherical harmonics of Eq. 2.27. A full description of this effect can be found in Ref. [16].

2.3.5 Experimental Access to Reciprocal Space

The theoretical framework presented so far will now be brought to the experimental realm, discussing typical RSXS experimental setups. To this effect, let us begin by visualizing the translation between a real space context of a diffraction experiment and its reciprocal space counterpart. Figure 2.12 shows on the left, and incident ray of X-rays into a sample (of tetragonal nature, common to the heterostructures investigated in this thesis). The light that has penetrated to the sample is eventually scattered following Eq. 2.6 in many different directions. The task of a diffraction experiment is to align the detector in such a way as to pick up the scattered signal. However, in systems of single orientation (single crystals and heterostructures), accessing a desired reflection requires more than just moving the detector: it involves moving the incident angle of the beam, i.e. rotating the sample with respect to the incoming beam. Moreover, the beam which is scattered in directions underneath the sample surface, the sample horizon, will be absorbed by the sample. The relationship given by Eq. 2.6 will yield information about the Bragg planes. Whether they be of structural or electronic origin, Bragg planes will result in points in reciprocal space. Their layout is shown on the right of Fig. 2.12. The reciprocal space vectors ($\vec{q}_x, \vec{q}_y, \vec{q}_z$) are defined by the crystal axes ($\vec{a}, \vec{b}, \vec{c}$), and the points below the sample horizon are shown as faded. They are accessible in tilted geometries, as described below. Finally, the momentum transfer $\vec{q} = (\vec{k}_{in} - \vec{k}_{out})$ is limited by the wavelength of the incoming X-rays. This limitation is also known as the Ewald sphere. For soft X-rays, the Ewald sphere is in the order of 0.1 \AA^{-1} , which is sufficient to probe Bragg planes with separation of at least $\sim 10 \text{ \AA}$.

2.3.5.1 Navigating in Reciprocal Space

Any position in \vec{q} -space can be reached by adjusting a set of angles in real space, essentially the angle of incidence and exit. In a multiple circle diffractometer, a direct translation between the angles and the position in \vec{q} -space can be calculated using the so-called orientation matrix [28]. For RSXS, where normally there is no structural Bragg peak within the Ewald sphere, the orientation matrix is defined in “virtual” terms. That is, the crystal systems are previously aligned and the angular directions are known. The heterostructures investigated throughout this thesis have

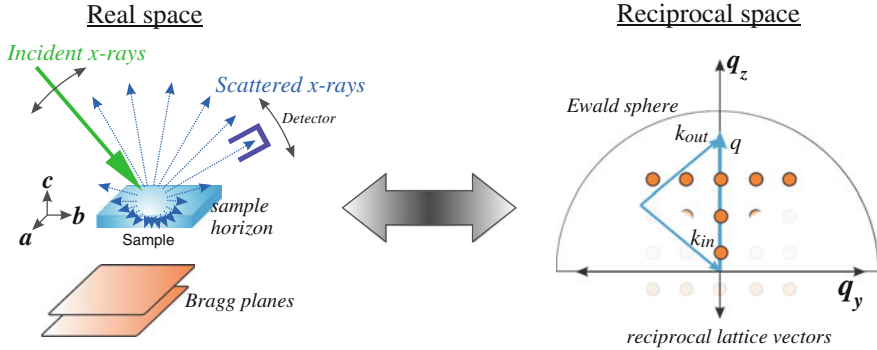


Fig. 2.12 The translation between real space (the experimental setup and the probed atomic positions) and reciprocal space, where the X-ray's provide the means to obtain the Fourier-transform of the Bragg planes. Navigating in reciprocal space corresponds therefore to scanning different combinations of the direction of incident beam, detector position

the advantage of withholding the overall substrate tetragonal symmetry. Even for cases when the systems are relaxed, the (a, b, c) directions are well-defined with respect to the macroscopic sample. Epitaxially grown heterostructures, however, cannot be polished along different crystal directions which can make accessing Bragg peaks below the sample horizon difficult.

Figure 2.13 shows a 3-dimensional pictograph of reciprocal space. The sample-horizon-blocked areas are shown by shaded blue spheres, as is the entire Ewald sphere (gray). Peaks of the kind $(0, 0, l)$ are reached by adjusting $(\omega, 2\theta)$ with the constraint $\omega = 2\theta/2$. Furthermore, there are essentially two ways to access a reciprocal lattice point with in-plane component $(0, k, l)$. First, setting 2θ to the value of θ given by Bragg's law. Then, an angular offset is introduced to the angle ω (χ) to introduce the value along q (h). The offset is given by

$$\alpha = \arccos \frac{(0, 0, l) \cdot (0, k, l)}{|(0, k, l)| |(0, 0, l)|}. \quad (2.36)$$

This schematic is outlined in Fig. 2.13. The geometry in which the offset is introduced in ω is *flat*, because the sample surface normal is in the scattering plane. On the other hand, placing the offset in χ yields a *tilted* scattering geometry. Figure 2.13 also shows that in a flat geometry, a φ -rotation of 90° (rotation about q_z) will invert the roles of ω and χ . Finally, to access reflexes of the kind (h, k, l) , a combination of all three angles ω, χ and φ is required. For example, accessing the $(1, 1, 1)$ direction, as we will see in later chapters, involves offsetting $\chi \rightarrow 55^\circ$ and $\varphi \rightarrow 45^\circ$. When doing this, the vector of interest (h, k, l) is placed into the scattering plane, but more importantly, that vector is now perpendicular to the φ -rotatable disc. This means that rotating φ will now rotate around (h, k, l) . However, the tilted geometry will have a disadvantage. As we will see in Chap. 3, this tilt will restrict the access to rotation around (h, k, l) .

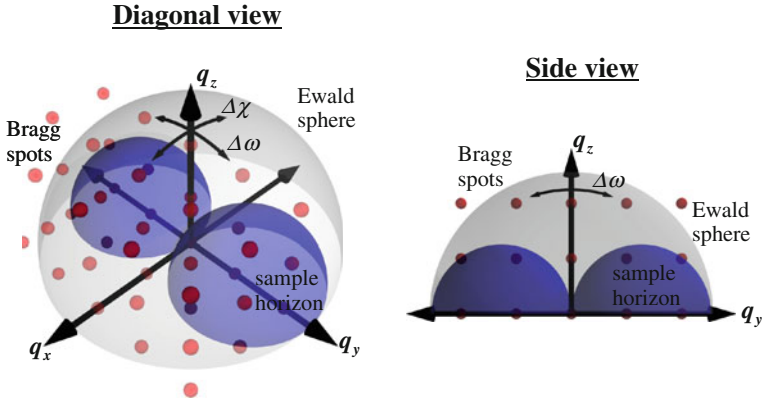
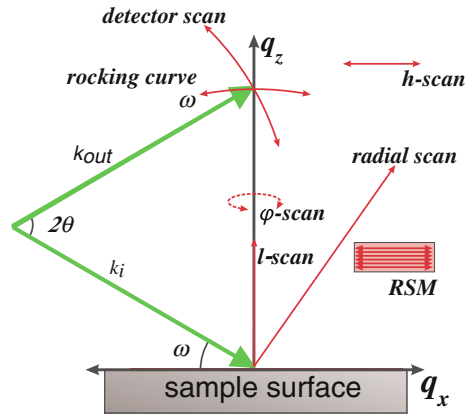


Fig. 2.13 (left) 3-dimensional pictograph of scans in reciprocal space. The in-plane directions can be accessed by offsetting ω or χ , while rotating φ and a combination of ω and χ will access positions of the kind (h, k, l) . (right) A typical sample horizon schematic when using the flat scattering geometry

Fig. 2.14 A schematic of how certain angular movements translate into RS, as well as some definitions of linear scans in defined directions. A RSM consists in an array of adjacent linear scans to map a 2D region in RS



The shape of Bragg reflex in RS can be visualized using the technique of reciprocal space mapping (RSM). Any diffraction measurement involves a scan of \vec{q} -values in RS. The method of RSM is essentially cutting several adjacent lines in RS in such a way as to record a 2-dimensional intensity map around the vicinity of a certain Bragg peak. This is discussed at length in Refs. [29, 30].

2.3.5.2 Bragg Reflex Topology

In practice, the rules given by Eq. 2.6 are relaxed for different values of (h, k, l) . In other words, real conditions of the sample and the experiment will give rise to broadened peaks. The main mechanisms of elongation common in heterostructures

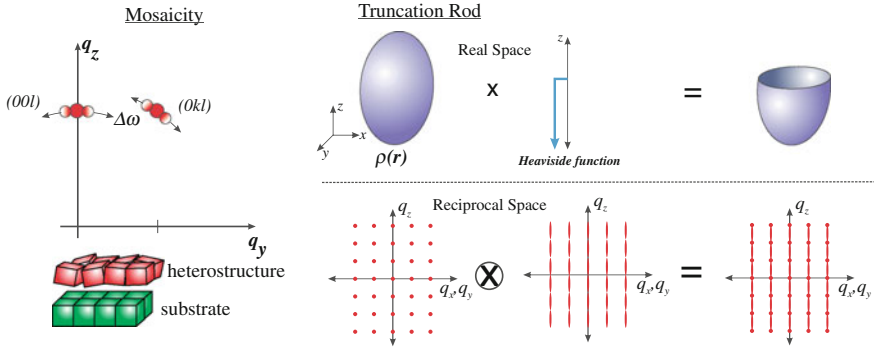


Fig. 2.15 (left) The concept of mosaicity involves domains of equal crystal orientation, which gives rise to a broadening along the ω direction. (right) A long broadening along the l -direction arising from the surface truncation

are mosaicity (mostly finite in-plane correlation), truncation rods, resolution of the experiment, and strong absorption. The latter is a consequence of the reduction of scatterers when the penetration depth is reduced. Strongly enhanced on resonance, quantifying a Bragg reflex's width as function of energy across a resonance can yield absorption coefficients in absolute units [31]. The experimental resolution is the smallest effect in many of today's sources.

Mosaicity arises when different portions of the sample are slightly misaligned with respect to others. In heterostructures, this can easily occur during the growth process. Introducing small misalignments of the unit cell with respect to the substrate implies the scattering in different directions at a given incident angle. Since the magnitude of \vec{q} is the same, the other scattering directions will all be along a centered at the origin, with radius $\sqrt{q_x^2 + q_y^2 + q_z^2}$. Scanning ω , also known as a rocking curve, is a common method of quantifying the degree of mosaicity in a sample. The angular width of a rocking curve corresponds to the amount of mosaicity in the sample. In heterostructures, the term mosaicity is commonly associated with the in-plane correlation length. That is, it refers to the size of laterally spaced domains with the same crystal orientation. The concept is shown visually in Fig. 2.15.

Heterostructures always possess a marked surface along z , which leads to an important inherent property: the crystal truncation rod. Taking the Fourier-transform of the product of the infinite (and periodic) $\rho(\vec{r})$ with a Heaviside function $h(z)$, one convolutes the Fourier-transforms of those functions. The Fourier transform of a step function like $h(z)$ is i/q_z , and thus the intensity is proportional to $1/q_z^2$. Combining this result with the delta functions of Eq. 2.6, one obtains streaks of intensity along the surface normal. This effect is shown visually in Fig. 2.15. Moreover, this effect is also present in any truncated crystal system, like the superconducting cuprates, as we will discuss in Chap. 4.

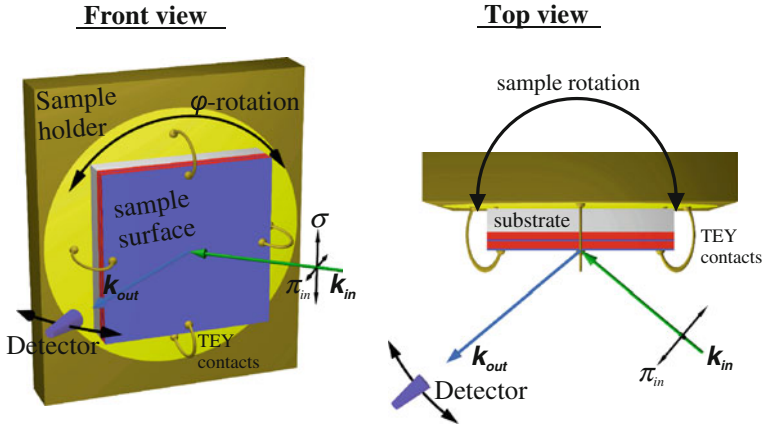


Fig. 2.16 A schematic of the two-circle diffractometer used in throughout this thesis

2.3.5.3 The experimental setup

The actual scattering geometry commonly used in RSXS is shown in Fig. 2.16. First of all, due to the large absorption cross section of air for X-rays of this wavelength [19], these experiments can only be done with operating pressures below 10^{-4} mbar. Thus, the entire experiments are enclosed in vacuum chambers. The simplest kind of diffraction setup offers 2 automated motors: the sample and detector rotation. Additionally, the setup can offer the option of mounting the sample on a rotatable disc (highlighted yellow in Fig. 2.16), which allows rotation around a vector perpendicular to the holder's back surface in the scattering plane.

When scattering in the flat geometry of Fig. 2.16, this corresponds to a φ -rotation. The measurement of the XAS is done by grounding the sample from the heterostructure to the holder, as indicated in Fig. 2.16 by wires connecting the sample surface.⁶ Then, when the light strikes the samples and releases photoelectrons, the grounded sample will replenish the exited electrons and register a current. This current measurement is normally called a “drain current” or total electron yield (TEY) signal.

The RSXS experiments of this thesis were done using the setup of the UE46-PGM1 beamline at BESSY in Berlin, shown in Fig. 2.17. The undulator at this beamline generates X-rays with variable polarization and energies in the range 200–1900 eV with a bandwidth of ≤ 1 eV. The beamline operates two end-stations, which can be run independently. The first one is an ultra-high vacuum diffraction chamber. It operates at pressures of around 10^{-10} mbar and is equipped with a continuous flow He cryostat. The temperature ranges that can be achieved are 10–350 K, although certain conditions can even allow lower temperatures (down to 3 K). Inside the chamber, there is a 2-circle diffractometer like the one depicted in Fig. 2.16. The sample motor

⁶ The substrates used to grow TMO heterostructures are insulating, so the grounding cannot be done through the substrate.

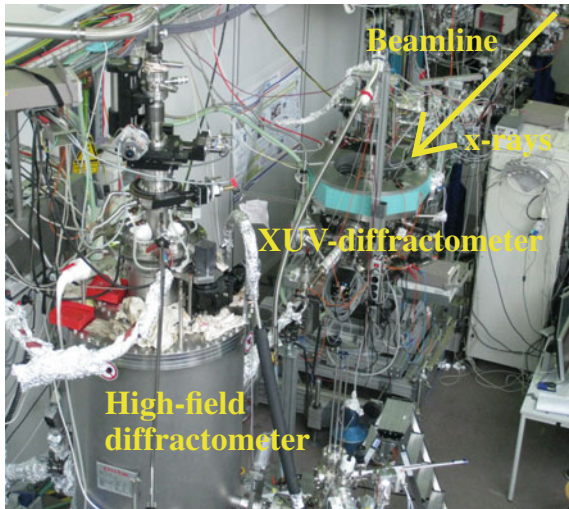


Fig. 2.17 The setup of the the UE46-PGM1 beamline at BESSY, in Berlin, Germany. The beamline operates two chambers: one predominantly for diffraction which Fig. 2.16 depicts, and one for magnetic circular dichroism (XMCD) experiments

(ω) and detector motor (2θ) rotations are essentially independent, with wide angular ranges accessible ($-30^\circ < \omega < 160^\circ$, $-50^\circ < 2\theta < 180^\circ$). The diffractometer, which is built on a very stable mount, has motorized movement in all three directions of the sample stage, and so allows maximum precision when measurement small samples. The φ -rotation of the sample is not motorized, in order to reach temperatures below 30 K. This rotation is done manually using a screw driver installed behind the sample holder. The precision of this rotation is about $\sim 5^\circ$. The drain signal is measured independently from the scattered signal.

The second end-station operating at UE46-PGM1 is a high-magnetic field chamber. A rotatable, superconducting magnetic coil can generate fields of up to 7T in any direction with respect to the sample surface. Whilst most of the experiments carried out in this end-station are XAS measurements of magnetic circular dichroism (XMCD), the chamber does possess a very unique feature. The chamber has rotatable sample and detector motors (ω and 2θ). This permits scattering experiments in high magnetic fields, albeit with certain limitations due to the rotatable magnet. Fixed slits provide windows in 2θ of $0^\circ < 2\theta < 66^\circ$ and $84^\circ < 2\theta < 96^\circ$. A schematic of the available scattering geometries under applied field with the magnet set at 0° is shown in Fig. 2.18.

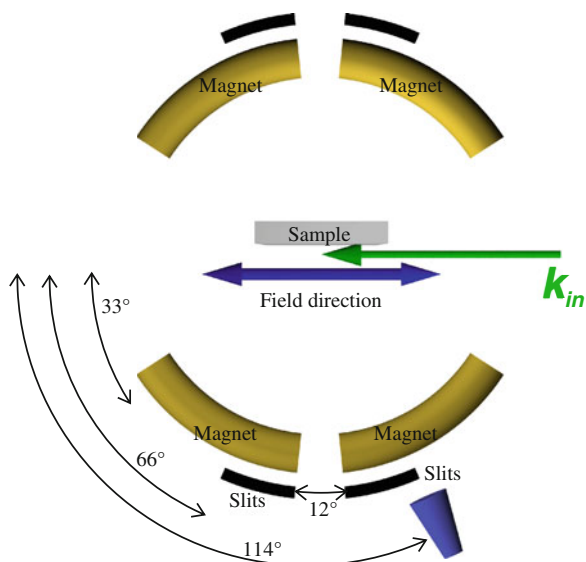


Fig. 2.18 A schematic of the scattering geometries available with applied magnetic field at the high-field station of the the UE46-PGM1 beamline at BESSY. The field direction rotates with the magnet

References

1. M. Blume, D. Gibbs, Polarization dependence of magnetic X-ray scattering. *Phys. Rev. B*, **37**, 1779–1789 (1988)
2. E. D. Isaacs, D.B. McWhan, D. Mills, D. Gibbs, D.R. Harshman, C. Vettier, Polarization and resonance properties of magnetic X-ray scattering in holmium. *Phys. Rev. Lett.* **61**, 1241 (1988)
3. J. Fink, E. Schierle, E. Weschke, J. Geck, Resonant elastic soft X-ray scattering. *Rep. Prog. Phys.* **76**, 056502 (2013)
4. C. Vettier, Resonant elastic X-ray scattering: Where from? where to? *Eur. Phys. J.* **208**, 3–14 (2012). (Special topics)
5. F. R. Elder, A.M. Gurewitsch, R.V. Langmuir, H.C. Pollock, Radiation from electrons in a synchrotron. *Phys. Rev.* **71**, 829–830 (1947)
6. J. A.-Nielsen, D. McMorrow, *Elements of Modern X-ray Physics* (John Wiley and Sons Ltd, New York, 2001)
7. A. Hofmann, *Synchrotron Radiation* (Cambridge University Press, Cambridge, 2004)
8. H. Wiedmann, *Synchrotron Radiation* (Springer, Berlin, 2003)
9. D.H. Templeton, L.K. Templeton, Polarized x-ray absorption and double refraction in vanadyl bisacetylacetonate. *Acta Cryst.* **A36**, 237–241 (1980)
10. J. P. Hannon, G.T. Trammell, M. Blume, D. Gibbs, X-ray resonance exchange scattering. *Phys. Rev. Lett.* **61**, 1245–1248 (1988)
11. P. Carra, B.T. Thole, Anisotropic X-ray anomalous diffraction and forbidden reflections. *Rev. Mod. Phys.* **66**, 1509–1515 (1994)
12. J. P. Hill, D.F. McMorrow, X-ray resonant exchange scattering: Polarization dependence and correlation functions. *Acta Cryst.* **A52**, 236–244, (1996)
13. C. J. Sparks, K. Fischer, G. Materlik, *Resonant Anomalous X-ray Scattering* (Elsevier, Amsterdam, 1994)

14. F. de Groot, G. van der Laan, Collected works of Theo Thole: the spectroscopy papers. *J. Electron Spectrosc. Relat. Phenom.* **86**, 25–40 (1997)
15. Y. Joly, S.D. Matteo, O. Bunău, Resonant X-ray diffraction: basic theoretical principles. *Eur. Phys. J.* **208**, 21 (2012). (Special topics)
16. M.W. Haverkort, N. Hollmann, I.P. Krug, A. Tanaka, Symmetry analysis of magneto-optical effects: the case of X-ray diffraction and x-ray absorption at the transition metal $L_{2,3}$ edge. *Phys. Rev. B* **82**, 094403 (2010)
17. M.W. Haverkort, Theory of X-ray resonant spectroscopy. Presentation at the UBC-Max Planck Summer School, 2011
18. S. Di Matteo, Multipole interpretation of resonant elastic X-ray scattering. Presentation at the REXS Conference, 2011
19. B. L. Henke, Atomic scattering factors (1993). http://henke.lbl.gov/optical_constants/asf.html
20. K. D. Finkelstein, Qun Shen, S. Shastri, Resonant X-ray diffraction near the iron K-edge in hematite ($\alpha - \text{Fe}_2\text{O}_3$). *Phys. Rev. Lett.* **69**, 1612–1615 (1992)
21. C. Cohen-Tannoudji, B. Diu, F. Laloe, *Quantum Mechanics* (Wiley, New York, 2006)
22. J. Chakhalian, J.W. Freeland, H.-U. Habermeier et al., Orbital reconstruction and covalent bonding at an oxide interface. *Science* **318**(5853), 1114–1117 (2007)
23. E. Benckiser, M.W. Haverkort, S. Brück et al., Orbital reflectometry of oxide heterostructures. *Nat Mater* **10**, 189–193 (2011)
24. J. Chakhalian, J. M. Rondinelli, Jian Liu, et al., Asymmetric orbital-lattice interactions in ultrathin correlated oxide films. *Phys. Rev. Lett.* **107**, 116805 (2011)
25. J. W. Freeland, J. Liu, M. Kareev et al., Orbital control in strained ultra-thin $\text{LaNiO}_3/\text{LaAlO}_3$ superlattices. *Europhys. Lett.* **96**(5):57004, (2011)
26. H. Ott, C. Schüßler-Langeheine, E. Schierle et al., Magnetic x-ray scattering at the M_5 absorption edge of ho. *Phys. Rev. B* **74**, 094412 (2006)
27. E. Schierle, V. Soltwisch, D. Schmitz et al., Cycloidal order of $4f$ moments as a probe of chiral domains in dymnO_3 . *Phys. Rev. Lett.* **105**, 167207 (2010)
28. W. R. Busing, H.A. Levy, Angle calculations for 3- and 4-circle X-ray and neutron diffractometers. *Acta Crystallogr.* **22**(4), 457–464 (1967)
29. T. Baumbach, U. Pietsch, V. Holy, *High-Resolution X-ray Scattering: From Thin Films To Lateral Nanostructures*, 2nd edn. (Springer, New York, 2001)
30. A. Frano, X-ray scattering investigations in transition-metal-oxide heterostructures. Master's thesis, Universität Stuttgart, 2010
31. S. Partzsch, S.B. Wilkins, E. Schierle et al., Resonant soft X-ray scattering studies of multiferroic YMn_2O_5 . *Eur. Phys. J.* **208**, 133–139 (2012). (Special topics)

Spin Spirals and Charge Textures in
Transition-Metal-Oxide Heterostructures

Frano, A.

2014, XIV, 149 p. 116 illus., 36 illus. in color., Hardcover

ISBN: 978-3-319-07069-8